Supplementary Information (SI) for Materials Chemistry Frontiers.
This journal is © the Partner Organisations 2026

Supporting Information

Cocoon-Inspired Gradient Mullite Nanofibrous Aerogels for Broadband Sound Absorption and Thermal Insulation

Junjiang Sima,[a] Fan Wu,*[b] Songchun Fang,[a] Yury A. Skorik,[c] Yi-Tao Liu,[a] Bin Ding*[d]

[a] State Key Laboratory of Advanced Fiber Materials, Innovation Center for Textile Science and Technology, College of Materials Science and Engineering, Donghua University, Shanghai 201620, China

[b] School of Materials Science and Engineering, Shanghai University of Engineering Science, Shanghai 201620, China. E-mail: wufansues@163.com

[c] Branch of Petersburg Nuclear Physics Institute named by B.P. Konstantinov of the National Research Centre «Kurchatov Institute» – Institute of Macromolecular Compounds, Bolshoi VO 31, St. Petersburg 199004, Russia

[d] School of Materials and Energy, Shanghai Polytechnic University, Shanghai 201209, China.

Email: binding@dhu.edu.cn

Supporting Information contains:

Supplementary Figure S1-S12, Equations Eqs1-Eqs6 and Table S1-S4

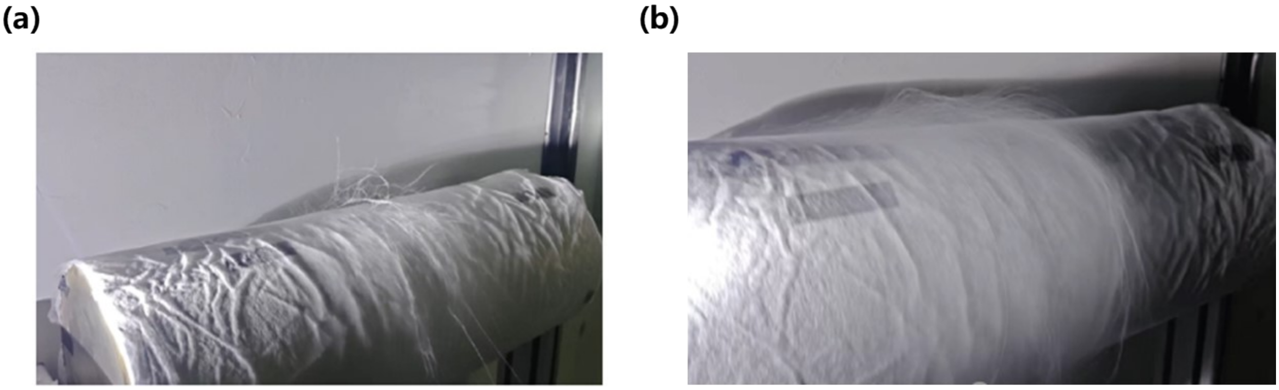

Figure S1. Optical photographs of the electrospinning collection process at (a) RH = 45% and (b) RH = 25%.

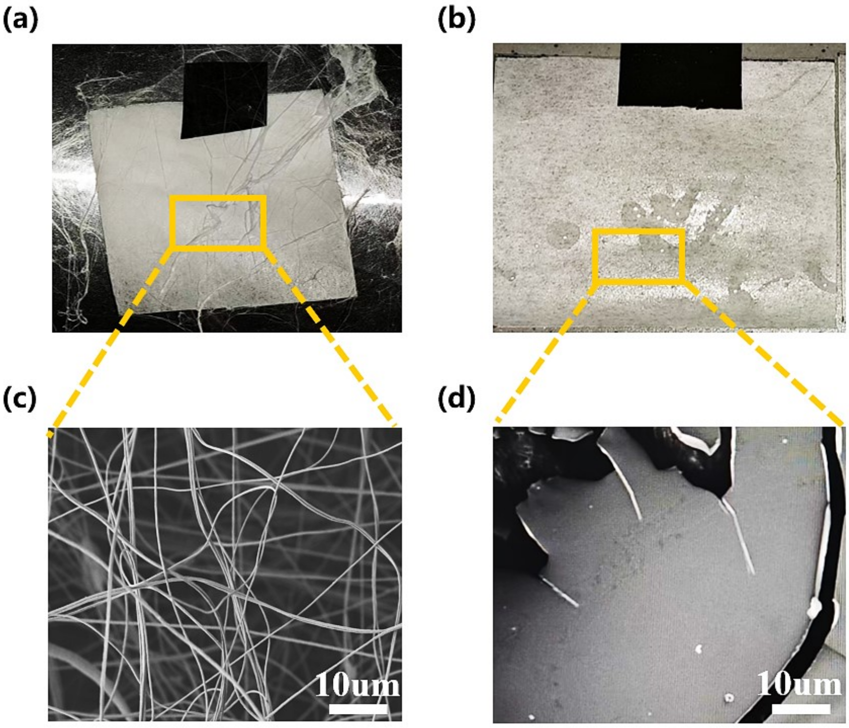

Figure S2. Optical and SEM observations of precursor deposition under different relative humidities. (a,b) Optical photographs of precursor deposits collected at a spinning distance of 3 cm under (a) 30% RH and (b) 50% RH. (c,d) SEM images of the corresponding deposits after standing for 1 h under (c) 30% RH and (d) 50% RH. The high-humidity condition suppresses fiber formation and leads to a gel-like morphology, supporting delayed gelation.

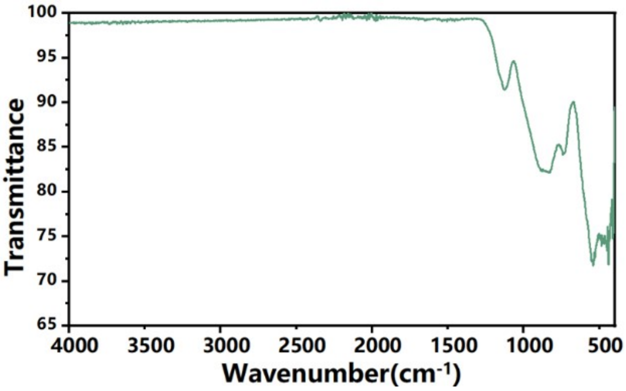

Figure S3. In the FTIR spectrum, the bands at 808 and 1089 cm⁻¹ are attributed to the vibrations of Si–O–Si and Si–O–Al bonds in the mullite-related aluminosilicate framework.

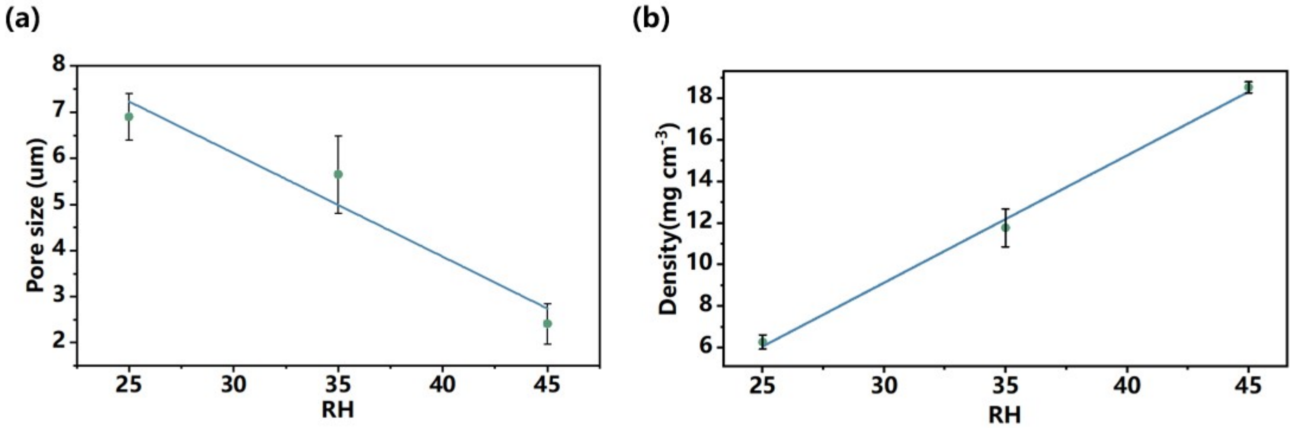

Figure S4. Empirical relationships between relative humidity (RH) and structural parameters: (a) average pore size and (b) bulk density. Error bars represent standard deviations.

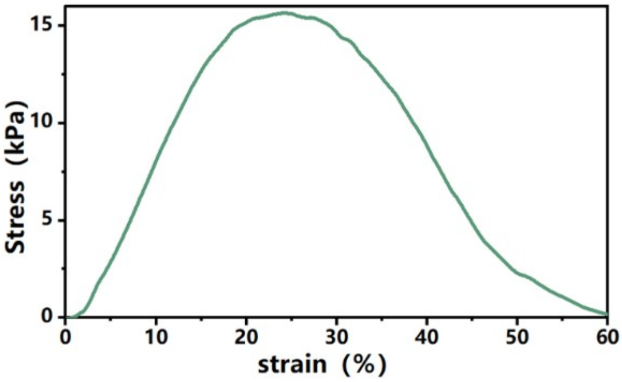

Figure S5. Tensile fracture curve of GMNF.

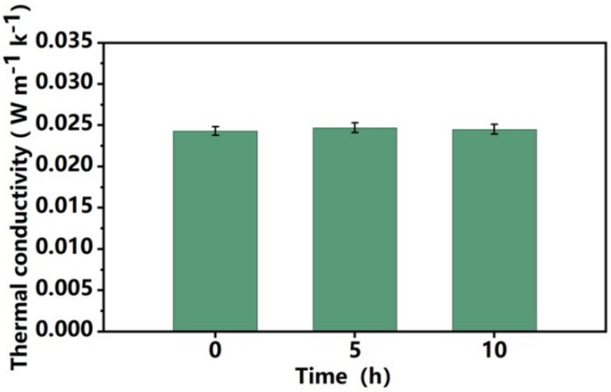

Figure S6. Thermal conductivity of GMNF after isothermal treatment at 1100 °C for different durations (0, 5, and 10 h). Error bars represent standard deviations.

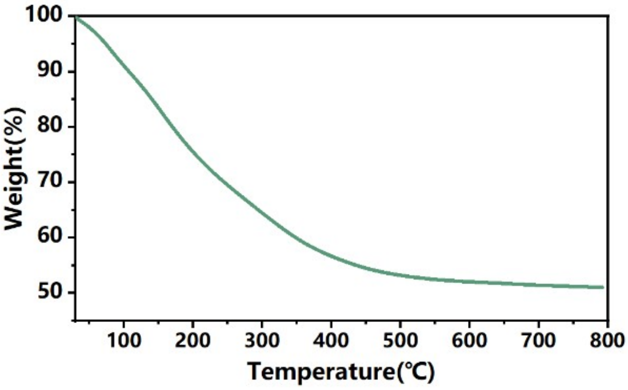

Figure S7. TG curve of GMNF.

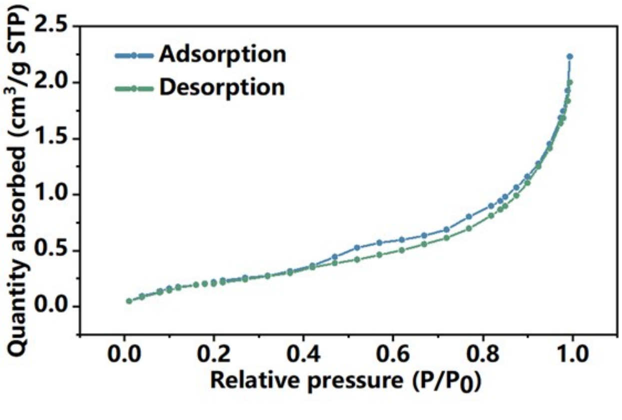

Figure S8. N_2 adsorption–desorption isotherm of GMNF.

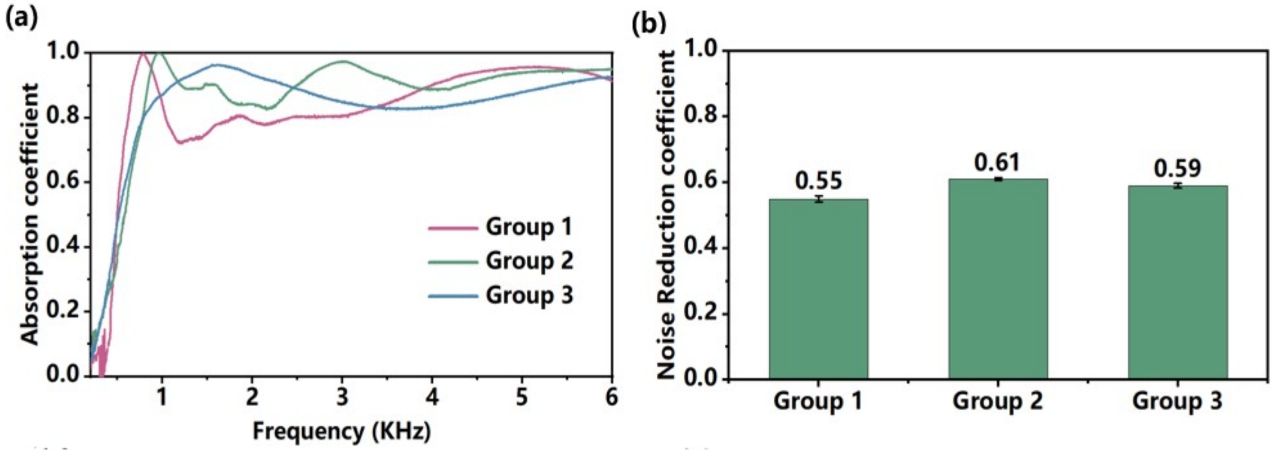

Figure S9. Sound absorption coefficients of samples with different structural configurations: (a) absorption coefficient curves; (b) corresponding average values.

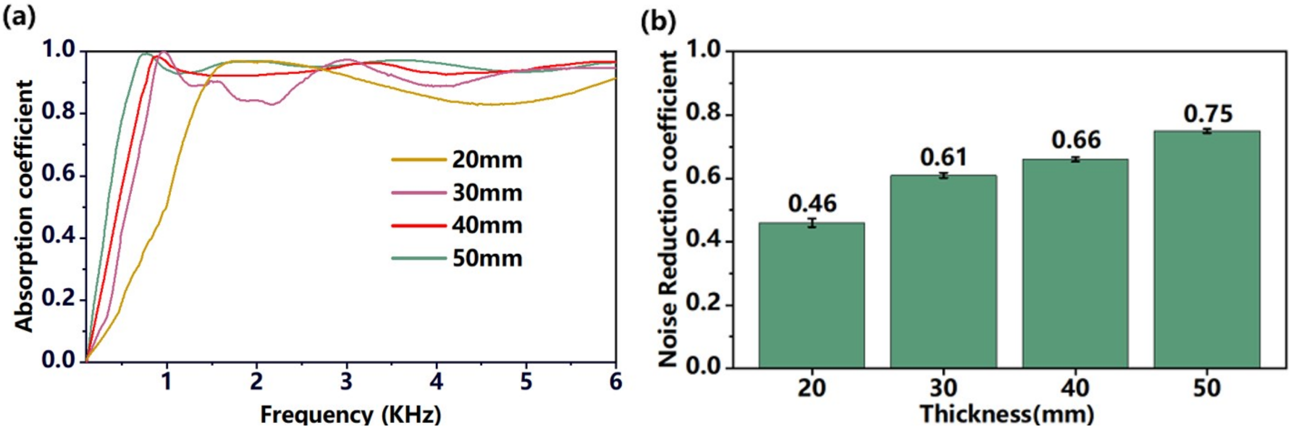

Figure S10. Sound absorption coefficients of samples with different thicknesses: (a) absorption coefficient curves; (b) corresponding average values.

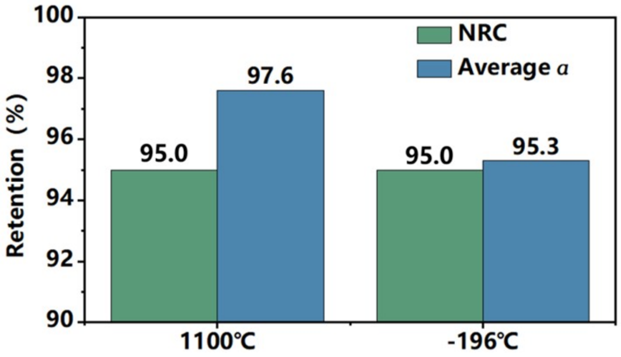

Figure S11. Retention of sound absorption performance after extreme-temperature treatments, calculated based on NRC and Average(α). The untreated sample is set as 100%.

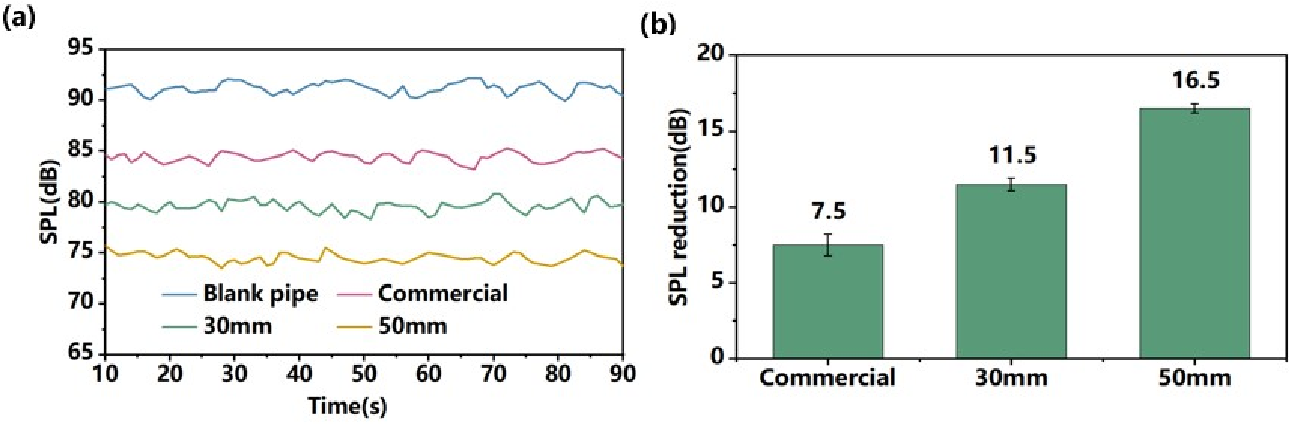

Figure S12. (a) Time-dependent SPL curves of the blank pipe, commercial acoustic cotton, and GMNF samples with different thicknesses under air compressor noise.(b) Corresponding SPL reduction values calculated from the average SPL of the blank pipe.

Supplementary Equations

Empirical relationships between relative humidity and structural parameters:

The dependence of bulk density and average pore size on the relative humidity (RH) can be expressed using linear regression as:

$$\rho = 0.613 \cdot RH - 9.255\left(R^2 = 0.996\right)\#（S1）$$

$$d =- 0.2245 \cdot RH + 12.844\left(R^2 = 0.939\right)\#（S2）$$

where ρ, d, and RH denote bulk density, average pore size, and relative humidity, respectively. Increasing RH leads to higher bulk density and reduced pore size, with strong linear correlations confirmed by the high R^2 values.

Thermal shielding efficiency calculation:

The thermal shielding efficiency (η) was calculated based on the steady-state temperature distribution using the following equation:

$$\eta = \frac{T_{hot} - T_{cold}}{T_{hot} - T_{ambient}} \times 100\%\#(S3)$$

where T_{hot}, T_{cold}, and $T_{ambient}$ represent the hot-side temperature, cold-side temperature, and ambient temperature, respectively. All temperatures were obtained under steady-state conditions during the butane flame heating test.

Classical surface impedance model for a rigidly backed porous layer:

For a rigidly backed single-density porous layer, the surface impedance is classically written as:

$$Z_s =- jZ_c cot\left(k_c d\right)\#（S4）$$

where Z_s, jZ_c, k_c, and d denote the surface impedance, characteristic impedance, complex propagation constant, and sample thickness, respectively. This expression indicates that the acoustic response is governed by both the intrinsic impedance characteristic and the propagation behavior within the porous layer. Consequently, structural variations can modify the frequency evolution of Z_s, which in turn affects the absorption peak position, bandwidth, and intensity.

Normalization method for radar chart:

To compare parameters with different units, all values were normalized using min–max scaling. For parameters with positive contribution, the normalized value was calculated as:

$$X' = \frac{X - X_{min}}{X_{max} - X_{min}}\#（S5）$$

For parameters with negative contribution, the normalized value was calculated as:

$$X' = \frac{X_{max} - X}{X_{max} - X_{min}}\#（S6）$$

where X', X', X_{min} and X_{max} denote the normalized value, original value, minimum value, and maximum value among the compared samples, respectively. Positive-contribution parameters refer to properties where higher values indicate better performance, while negative-contribution parameters refer to properties where lower values are preferred

Supplementary Tables

Table S1. Comparison of fabrication strategies and acoustic–thermal performance of representative porous fibrous materials

Material	Strategy	Thermal Conductivity (W m^{-1} K^{-1})	NRC	REF
Gradient Mullite Nanofibrous Aerogels	One-step electrospinning	0.024	0.61	This work
Gradient PSU/PVDF Micro/Nanofibrous Sponges	Multi-stage electrospinning	—	0.53	1
PU/PS Composite Fibrous Sponges	Multi-stage electrospinning	—	0.57	2
AS-Based Aerogel Fiber Metafabrics	Multi-stage electrospinning	0.029	0.57	3
Porous PMMA Fibrous Sponges	Multi-stage electrospinning	—	0.57	4
CNC-Based Dual-Network Ceramic Nanofibrous Aerogels	Freeze-drying-based fabrication	—	0.58	5
Bilayer-Coupled SiO_2 Nanofibrous Aerogels	Freeze-drying-based fabrication	—	0.58	6
Multiscale Composite Nanofibrous Aerogels	Freeze-drying-based fabrication	0.028	0.40	7
Multistage-Porous Aramid Nanofibrous Aerogels	Freeze-drying-based fabrication	0.037	0.52	8
SiO_2 Nanofiber-Based Aerogel Fiber Papers	Freeze-drying-based fabrication	0.035	<0.6	9
Graphene Aerogel	Freeze-drying-based fabrication	0.023	0.50	10

Table S2. Performance comparison between GMNF and other high-temperature-resistant porous ceramic fibers.

Material	Density (mg cm^{-3})	Thermal Conductivity (W m^{-1} K^{-1})	REF
Gradient Mullite Nanofibrous Aerogels	15	0.024	This work
$BaTiO_3/Al_2O_3$ aerogel	30	0.028	11
Silica/Zirconia aerogel	120	0.034	12
Al_2O_3 fiber reinforced ceramic	130	0.036	13
Mullite fiber phenolic aerogel	52	0.310	14
SiC aerogel	19	0.023	15
SiC /SiO_2 aerogel	40	0.026	16

Table S3. Layer thickness distribution of samples with different structural configurations

Group	**RH=25**	**RH=35**	**RH=45**
1	2mm	15mm	13mm
2	5mm	15mm	10mm
3	10mm	10mm	10mm

Note: The thickness of each layer was controlled during fabrication, and the reported values represent the designed thicknesses.

Table S4. Detailed data of the materials used in Fig. 4h

Material	**Density (mg cm^{-3})**	**Thermal Conductivity (W m^{-1} K^{-1})**	**maximum service temperature**	**NRC**	**REF**
Gradient Mullite Nanofibrous Aerogels	15.00	0.024	1100	0.61	This work
SiO_2/Polyarylether Aerogel	24.15	0.028	400	0.51	17
Commercial Glass Wool	20.00	0.028	500	0.56	Measured in this work
Rubber Aerogel	91.00	0.035	250	0.56	18
Pectin Aerogel	50.00	0.032	105	0.41	19
Graphene Aerogel	17.30	0.023	350	0.50	10
Natural Biodegradable Fiber	27.00	0.048	355	0.41	20
Mullite Aerogel	72.00	0.030	1000	0.56	21

Reference

1 Y. Feng, D. Zong, Y. Hou, X. Yin, S. Zhang, L. Duan, Y. Si, Y. Jia and B. Ding, Gradient structured micro/nanofibrous sponges with superior compressibility and stretchability for broadband sound absorption, *J. Colloid Interface Sci.*, 2021, **593**, 59-66.

2 X. Xu, C. Liu, S. Zhang, J. Yu and B. Ding, Dual-scale pore structured composite fibrous sponges with enhanced waterproof properties for high-efficiency broadband noise absorption, *Compos. Commun.*, 2025, **58**, 102541.

3 L. Huang, Y. Tian, F. Wu, X. Yin, R. A. Surmenev, J. Yu, Y.-T. Liu and B. Ding, Multiscale Pore-Structured Aerogel Fiber Metafabric for High-Performance Noise Reduction and Thermal Insulation, *ACS Appl. Polym. Mater.*, 2025, **7**, 6262-6271.

4 Z. K. Ding, M. Geng, S. Wang, H. L. Liu, X. Yin and J. Y. Yu, Direct synthesis of lightweight fiber sponges with interconnected nanopores structured fibers for absorbing low-frequency noise, *J. Text. Inst.*, 2025, **116**, 971-979.

5 D. D. Zong, W. Y. Bai, X. Yin, J. Y. Yu, S. C. Zhang and B. Ding, Gradient Pore Structured Elastic Ceramic Nanofiber Aerogels with Cellulose Nanonets for Noise Absorption, *Adv. Funct. Mater.*, 2023, **33**, 2301870.

6 Y. N. Sun, D. D. Zong, Y. Z. Li, S. Y. Pang and Y. Liu, Owl-Inspired Coupled Structure Nanofiber-Based Aerogels for Broadband Noise Reduction, *ACS Appl. Mater. Interfaces*, 2025, **17**, 34387-34395.

7 Y. Y. Wang, X. Q. Yin, N. Pang, X. M. Yuan, Q. Han, M. J. Yu, C. G. Wang and C. J. Zhou, Biomimetic all-fiber hierarchical multiscale composite aerogels for multifunctional thermal, acoustic, and oil absorption applications, *Compos. Sci. Technol.*, 2026, **274**, 111445.

8 R. Yan, W. F. Qin, G. C. Gong, W. Chen, H. Peng and B. Zhou, Lightweight Composite Aramid Nanofiber Aerogel With Multistage Pores and Layered Structure for Acoustic and Thermal Insulation, *J. Appl. Polym. Sci.*, 2025, **142**, e56850.

9 W. Y. Bai, D. D. Zong, X. Y. Liu, F. Wang, X. Yin, J. Y. Yu, S. C. Zhang and B. Ding, Flame-retardant, ultralight, and superelastic electrospun fiber sponges for effective sound absorption, *J. Text. Inst.*, 2024, **115**, 724-732.

10 Y. J. Zhao, K. X. Zeng, N. Ahmad, W. Zhou, Z. G. Wang and W. Zhai, Gradient graphene aerogels for broadband noise absorption with robust environmental durability, *Chem. Eng. J.*, 2025, **525**, 170429.

11 Y. Gao, P. H. Yu, J. Zhang, G. D. Zhang, C. H. Guo, Y. Q. Zhou, Y. Z. Long and H. Wu, Compressible Piezoelectric Ceramic Nanofiber Aerogels with Multifunction, *Adv. Fiber Mater.*, 2025, **7**, 937-949.

12 C. Wu, J. Jiang, C. Dong, L. Zhao, J. Liu, C. Liu, H. Deng, K. N. Hui, H. Pang, Y. Yan and M. Liu, Remarkably Enhance the Stealth/Resistance/Mechanical Properties of Silica-Zirconia Ceramic Aerogel by Phase Transitions and Interface Evolution, *Adv. Funct. Mater.*, 2025, **35**, 2505742.

13 Y. Cheng, Y. Chen, X. Hu, L. Liu, X. Ye, J. Zhang, X. Ma and J. Wang, Ceramic Matrix Composites as Self-Standing Monoliths and Coatings for Thermal Superinsulation and Passive Daytime Radiative Cooling, *Adv. Funct. Mater.*, 2025, **35**, 2504931.

14 W. Wang, R. Liu, X. Jin, G. Liu, J. Zheng, C. Hong and X. Zhang, Exceptionally ablation-resistant lightweight ceramic fiber-reinforced Si-PR aerogel composites based on a ceramic biphasic system, *Compos. Part B Eng.*, 2026, **311**, 113282.

15 Y. Xia, G. Chen, Z. Zhang, S. Zhao, H. Lu, S. Deng and Z. Yang, Nanowire-filled layered SiC aerogels with excellent thermodynamic properties for thermal insulation at ultrahigh temperatures, *Chem. Eng. J.*, 2025, **510**, 161479.

16 P. Zhang, S. Zhao, K. Li, Z. Zhang, F. Yang, X. Li, Y. Song, Z. Gan and Z. Yang, Large-scale production of elastic SiC/SiO_2 nanofibrous composite aerogels with a labyrinth structure for high-temperature insulation, fire prevention, and noise absorption, *Chem. Eng. J.*, 2025, **505**, 159166.

17 Y. Cai, D. Ding, M. She, J. Wang, S. Yang, Q. Tang, H. Wang and S. Xiong, Sustainably designed SiO_2/polyarylate nanofiber composite aerogels for advanced thermo-acoustic insulation, *Compos. Part A Appl. Sci. Manuf.*, 2025, **196**, 109014.

18 Q. B. Thai, R. O. Chong, P. T. T. Nguyen, D. K. Le, P. K. Le, N. Phan-Thien and H. M. Duong, Recycling of waste tire fibers into advanced aerogels for thermal insulation and sound absorption applications, *J. Environ. Chem. Eng.*, 2020, **8**, 104279.

19 F. X. Zou, J. Cucharero, Y. J. Dong, P. J. Kangas, Y. Zhu, J. Kaskirinne, G. C. Tewari, T. Hänninen, T. Lokki, H. Li and J. Vapaavuori, Maximizing sound absorption, thermal insulation, and mechanical strength of anisotropic pectin cryogels, *Chem. Eng. J.*, 2023, **462**, 142236.

20 J. Liao, Y. Hou, J. Li, M. Zhang, Y. Dong and X. Chen, Lightweight and recyclable hybrid multifunctional foam based cellulose fibers with excellent flame retardant, thermal, and acoustic insulation property, *Compos. Sci. Technol.*, 2023, **244**, 110315.

21 W. Li, F. He, H. Liu, Y. Jiang, Y. Mu, C. Wang, X. Zhou, S. Jiang, L. Xu, L. Wang, X. He and M. Li, Electric Field-Induced Ordered-Structural Aerogels Enable Superinsulation and Multifunctionality, *Small*, 2024, **20**, e2406188.